Chapter 4 High efficiency $Al_xGa_{1-x}As/Si$ (x=0~0.22) two-terminal monolithic tandem solar cells

4-1 Introduction

For the practical use of solar cells, a two-terminal configuration is preferable. The theoretical analysis indicates that tandem solar cell with preferred bandgap structure configuration has conversion efficiency over 30%. [1)] Some tandem solar cells have been investigated for more than a decade in the search for a system capable of achieving high-efficiency. Such as, $Al_xGa_{1-x}As/GaAs$,[2)] GaInP/GaAs,[3)] $InP/Ga_xIn_{1-x}As$,[4)] and GaAs/Ge tandem solar cells.[5)] From the development of GaInP/GaAs (29.5%, AM1.5) tandem solar cell recently,[6)] it is expected that efficiency over 30% with a novel tandem solar cell configuration will be realized in near future.

The AlGaAs top cell has already been shown to have excellent radiation resistance,[7), 8)] and it is important for space application. When Si is considered as a bottom cell material, AlGaAs is a very attractive candidate for top cell material, of which bandgap is varied by changing the Al composition easily. So, the photocurrent of the top cell and the bottom cell can be matched by varying the Al composition. For two-terminal tandem solar cell, the photocurrent in the two cells must be equal for optimal operation, i.e., the top cell material should have a bandgap of 1.75 to 1.80 eV, in which range of x is about 0.2. In the chapter 2 of this dissertation, the theoretical calculation shows the optimal value of x is 0.21 for the photocurrent matching of the top

cell and the bottom cell.

$Al_{0.2}Ga_{0.8}As/Si$ mechanically-stacked cascade solar cells have been studied.[9] 1 sun, AM0, 17 % (active-area) efficient p^{+}-n $Al_{0.2}Ga_{0.8}As$ solar cell grown on GaAs substrate was obtained by low-pressure MOCVD, and the Voc of 1.22 V and fill-factor of 0.865 are close to ideal, the AM0 conversion efficiency could be increased further (to~20%) through improvement in Jsc values. The efficiency of the $Al_{0.2}Ga_{0.8}As/Si$ stacked tandem solar cell reached to 21% under AM1.5 conditions.[10] This tandem solar cell has a lower efficient Si bottom cell in comparison with that of the monolithic $Al_{0.22}Ga_{0.8}As/Si$ tandem solar cell in our study.

However, for the monolithic tandem solar cell, the AlGaAs top cell is grown on Si substrate with a p-n junction directly. There are significant lattice mismatch (~4%) and the thermal expansion coefficient mismatch between AlGaAs and Si, and the performance of AlGaAs/Si solar cell is poor because of the existence of high dislocation density in AlGaAs heteroepitaxial layer and the difficulty in the photocurrent mismatching between the top and the bottom cells. These have limited the efficiency of the tandem solar cell or single-junction solar cell to raise up to the theoretical efficiency. On the other hand, AlGaAs is sensitive to oxygen-related defects.[11] The quality of AlGaAs layer is also effected by moisture and oxygen in the growth ambient and source gases (AsH_3, and dopant) and organometallic sources (trimethylgallium and trimethylaluminum).[12] With increase of Al composition, the minority carrier lifetime of AlGaAs layer

decreases rapidly.[13)]

In this dissertation, we demonstrate the improvements of AlGaAs/Si (x=0.1～ 0.22) monolithic tandem solar cells fabricated by MOCVD. The improvements are performed using the suitable thermal cycle annealing (TCA) procedure and suitable growth temperature, and utilizing the back surface field (BSF) structure. The measured AM0 efficiency (active-area) of 19.0 % has been obtained by using the $Al_{0.15}Ga_{0.85}As/Si$ tandem solar cell under AM0 condition in two-terminal configuration.

Chapter 4-2 Sample fabrication

4-2-1 Si bottom cell

Prior to the growth of the $Al_xGa_{1-x}As$ top cell on Si, the thermal diffusion method with spin-coating of the diffusion sources was adopted to fabricate p^+-n-n^+ Si solar cells. First, n-type Si substrates oriented (100) 2° off toward [011] (P doped, $8x10^{15}$ cm^{-3}) were cleaned in the organic solution with the ultro sonic waves method, following the chemical etching with the acid solution (H_2SO_4+H_2O_2+H_2O=4:1:1; HF+H_2O=1:10). Next, after the spin-coating of the B diffusion source, the pre-baking process were carried out at 60 ℃ for 30 min in the air and at 600 ℃ in O_2 atmosphere for 20 min, respectively. Thermal diffusion of B was done at 1000 ℃ for 10 min. in N_2 atmosphere. The carrier concentration and the thickness of the p^+-type layer are 6×10^{19} cm^{-3} and 0.5 μm, respectively. Then, after etching off the oxide film on the Si front and rear surfaces, the back-surface-field (BSF) structure was formed with P-thermal diffusion at 900 ℃ for 30 min. using the procedure similar to the B diffusion method. The carrier concentration and the thickness of the n^+-type layer are 4×10^{19} cm^{-3} and 0.8 μm, respectively. And then, this p^+-n-n^+ Si solar cell was used as a substrate for growing the AlGaAs top cell on it.

4-2-2 $Al_xGa_{1-x}As$ top cell

$Al_xGa_{1-x}As$ top cell on Si for the two-terminal tandem solar cell consists of GaAs buffer layer, n^+-AlGaAs back surface field (BSF) layer, n-AlGaAs base layer, p^+-AlGaAs emitter layer, p^+-$Al_{0.8}Ga_{0.2}As$ window layer and p^+-GaAs contact layer. In the case of Al composition x=0, the GaAs top cell consists of GaAs buffer layer, n^+-$Al_{0.4}Ga_{0.6}As$ spacer, n^+-GaAs BSF layer, n-GaAs base layer, p^+-GaAs emitter layer, p^+-$Al_xGa_{1-x}As$ graded bandgap layer and p^+-GaAs contact layer. In order to improve the crystallinity of the heteroepitaxial layer, two-kinds of growth sequences were employed. Sequence (a) is same as the sequence (a) described in Chapter 3-2-2. Sequence (b) is shown in Fig. 4-1. The growth temperature of the AlGaAs top cell structure are 750 ℃ for sequence (a) and 800 ℃ for sequence (b), respectively. The AlGaAs top cell was grown on the Si substrate with the p^+-n-n^+ structure by an RF-heated horizontal metal-organic chemical vapor deposition (MOCVD) apparatus using the two-step growth technique. TCA was carried out 5 times during the growth process of the n^+-$Al_xGa_{1-x}As$ buffer layer. The defect density of the $Al_xGa_{1-x}As$ solar cell on Si was evaluated by the electron-beam-induced current (EBIC) image.

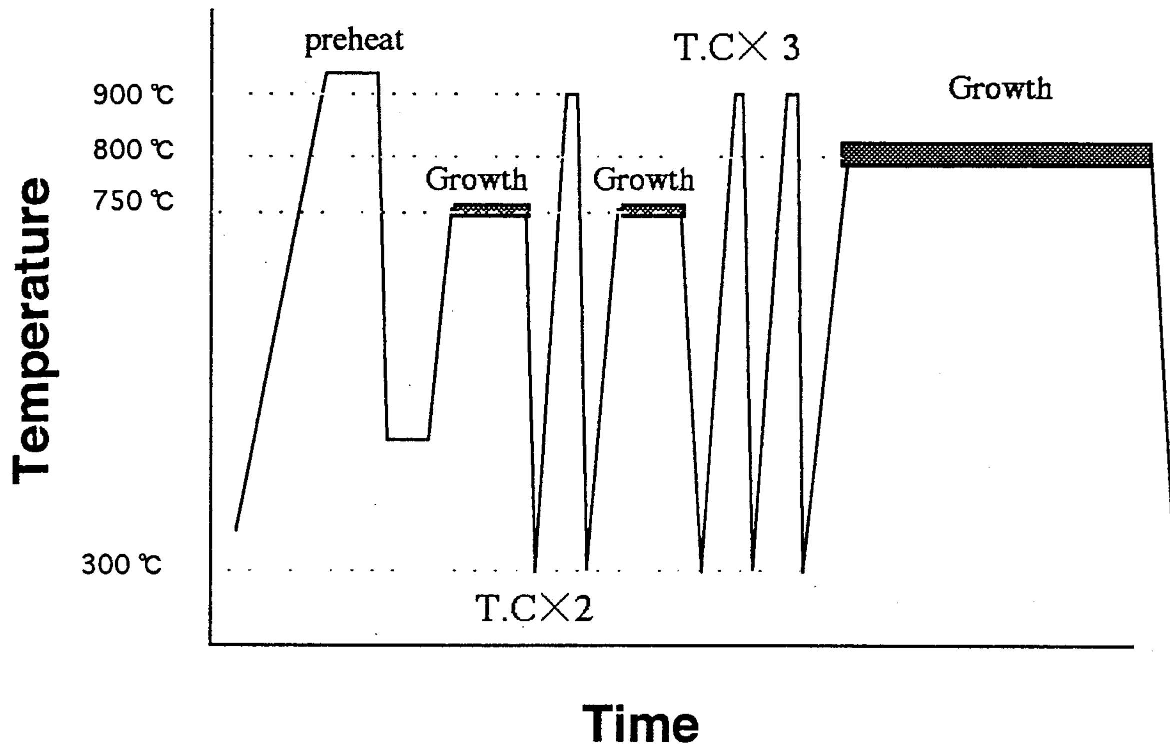

(b)

Fig. 4-1 The growth sequence of the AlGaAs top cell on Si.

750 ℃ growth for the AlGaAs buffer layer,

800 ℃ growth for the structure of the AlGaAs top cell.

Fig. 4-2 Schematic cross-sectional structure of the AlGaAs/Si tandem solar cell.

4-2-3 Structure of the tandem solar cell

After the growth, the electrodes for the p^+-GaAs layer, p^+-Si layer and n^+-Si layer were formed by evaporating AuZn/Au, Au and AuSb/Au, respectively. The antireflection films were formed by evaporating ZnS (50 nm) and MgF_2 (70 nm) double layers. The characteristics of the 2-terminal tandem solar cell were measured between AuZn/Au and AuSb/Au electrodes. The Au electrode on the p^+-Si layer was used to measure the individual characteristics of the top cell and the bottom cell. Fig. 4-2 shows the schematic cross-sectional structure of the $Al_{0.15}Ga_{0.85}As$ two-terminal tandem solar cell. The total area of the top cell and the bottom cell are both 5 $\times$5 mm^2. The conversion efficiency (η) and the short-circuit current density (Jsc) are the active area values. The current-voltage (I-V) characteristics were measured under AM0, 135.3 mW/cm^2 illumination (1sun) at 27 ℃ with a solar simulator.

Chapter 4-3 Photovoltaic properties

4-3-1. Si bottom cell, $Al_xGa_{1-x}As$ top cell and their connection

4-3-1-1. Si bottom cell

A Si solar cell with BSF structure was fabricated to improve the quantum efficiency of the Si bottom cell in the long-wavelength region, which is important for the AlGaAs/Si tandem solar cell. Fig. 4-3 shows the quantum efficiencies of the Si solar cells with and without BSF. The spectral response shifts toward the long-wavelength side with use of the BSF structure. The conversion efficiency of the Si cell without BSF is 10.1%; on the other hand, that of the Si solar cell with BSF is up to 11.3 % (without passivation or AR film). The I-V characteristic data are shown in Table 4-1.

Table 4-1
Current-voltage data of the Si solar cells with and without BSF.

Si solar cell	Jsc(mA/cm^2)	Voc(V)	FF (%)	η (%)
Without BSF	30.6	0.579	77.9	10.2
With BSF	32.7	0.591	79.1	11.3

The quantum efficiencies of the Si bottom cells with BSF and without BSF after the growth of the $Al_{0.15}Ga_{0.85}As$ top cell are evaluated with the formation of AR coating. The result is shown in Fig. 4-4. It is clear that the quantum efficiency in the long-wavelength region has been improved by BSF even in the tandem solar cell structure.

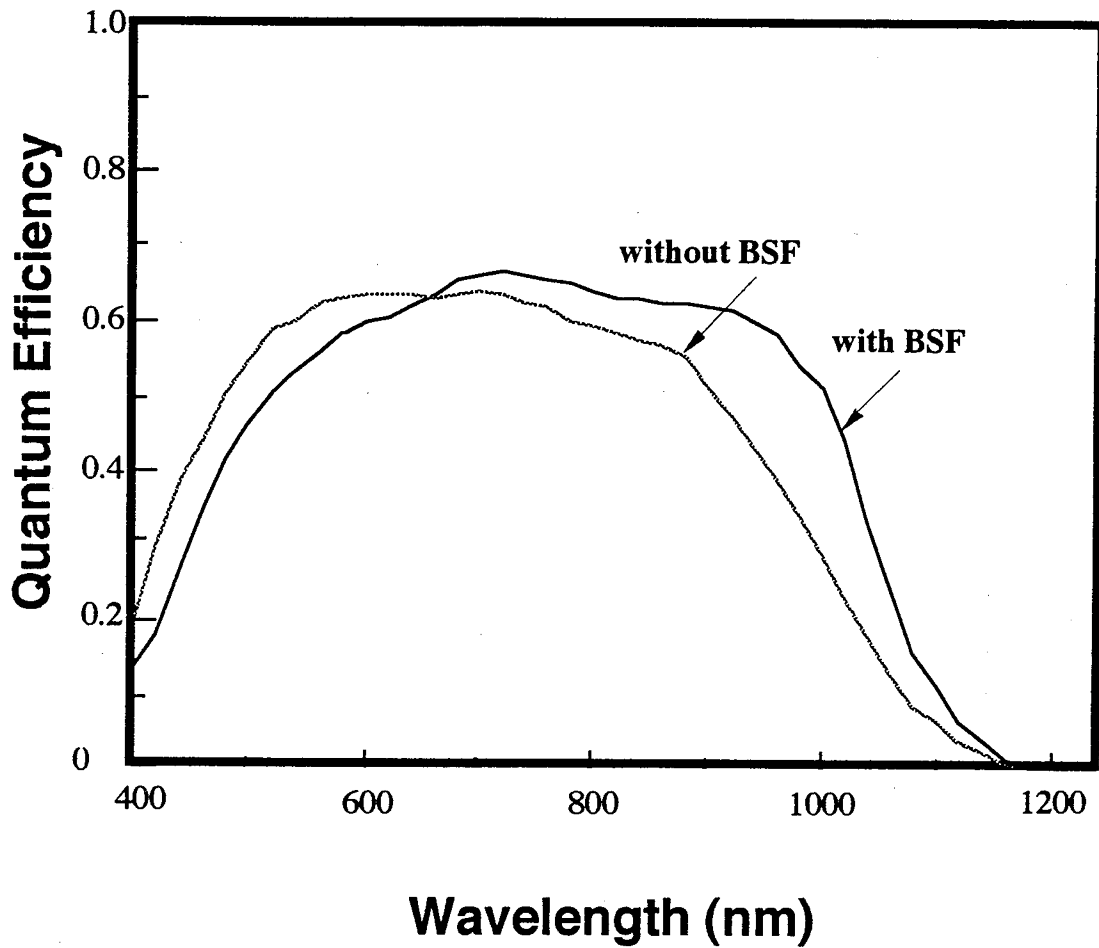

Fig. 4-3 The quantum efficiencies of the Si solar cells with and without BSF.

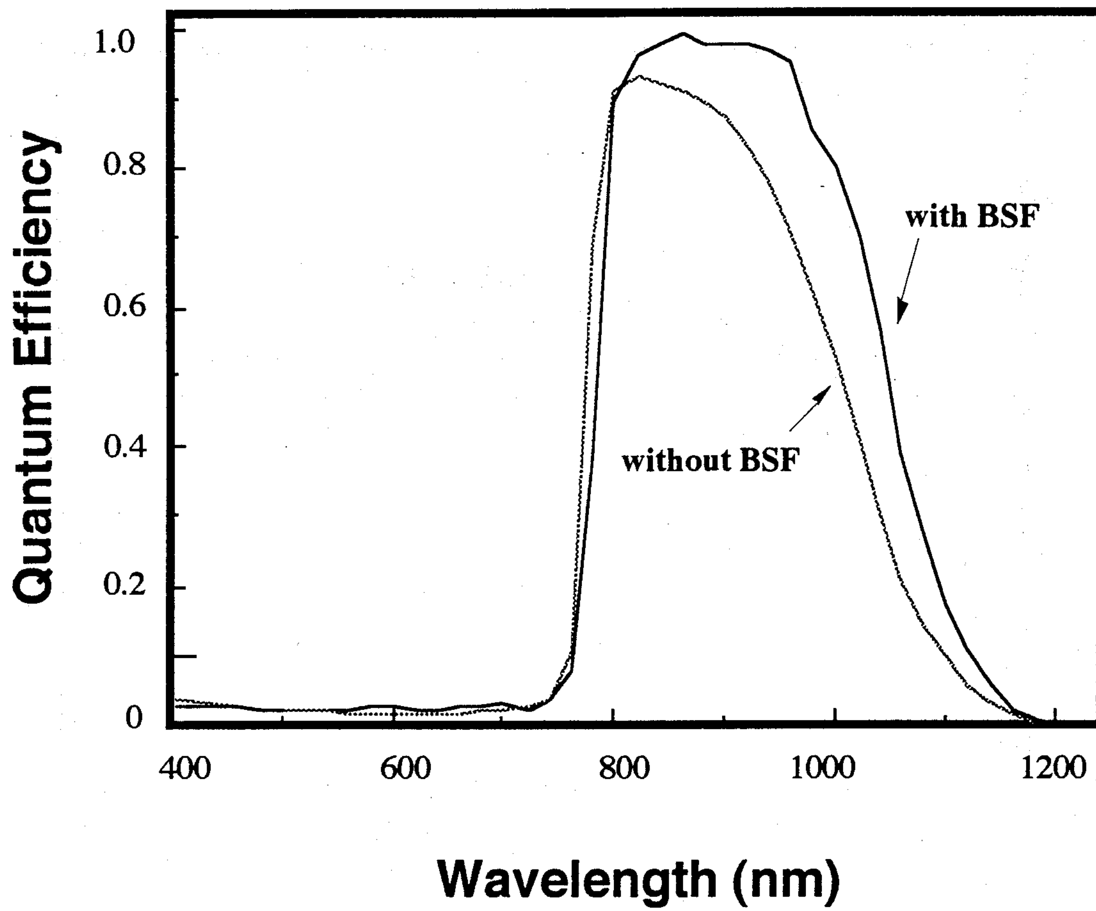

Fig. 4-4 The quantum efficiencies of the Si bottom cells with BSF and without BSF under the $Al_{0.15}Ga_{0.85}As$ top cell.

4-3-1-2. $Al_xGa_{1-x}As$ top cell

Table 4-2 shows the photovoltaic properties of the $Al_{0.1}Ga_{0.9}As$ and $Al_{0.22}Ga_{0.78}As$ solar cells on the Si substrate and DSD (dark spot density) of the EBIC image grown under sequence (a) and sequence (b). The conversion efficiencies of the $Al_{0.1}Ga_{0.9}As$ and $Al_{0.22}Ga_{0.78}As$ solar cells are increased from 10.2% to 11.5% and from 7.68% to 8.33%, respectively, by changing the growth sequence from (a) to (b). These improvements are due to the reduction of the dislocation density since the DSD is reduced. It is clear that high growth temperature (800℃) and high annealing temperature (300～900℃) are effective in increasing the efficiency.

Table 4-2
Photovoltaic characteristics of the $Al_{0.1}Ga_{0.9}As$ and $Al_{0.22}Ga_{0.78}As$ solar cell on Si under the growth sequences (a) and (b) (η: the active-area efficiency).

	Jsc (mA/cm^2)	Voc (V)	FF (%)	η (%)	DSD (cm^{-2})	Sequence
$Al_{0.1}Ga_{0.9}As$	21.3	0.905	71.6	10.2	1.6×10^7	(a)
	24.5	0.918	69.8	11.5	1.1×10^7	(b)
$Al_{0.22}Ga_{0.78}As$	13.3	1.02	75.9	7.68	2.5×10^7	(a)
	15.6	1.02	70.6	8.33	2.0×10^7	(b)

4-3-1-3. Connector between the top cell and the bottom cell

For the $Al_xGa_{1-x}As$/Si two-terminal tandem solar cell, it is necessary to provide an n^+-GaAs/p^+-Si tunnel heterojunction

connecting the AlGaAs top cell and the Si bottom cell. Because there is 4% difference in the lattice constants between GaAs and Si, the state density at the interface of GaAs/Si should be high, which is similar to the interface of Ge/Si.[14] These boundary states not only bend the part of energy band at the interface, but also cause the recombination in the boundary region. Fig. 4-5 shows a schematic band structure of the n^+-GaAs/p^+-Si tunnel heterojunction. The properties of n^+-GaAs/p^+-Si are dominated by the interface states. The I-V characteristic of the heterojunction would not be a standard tunnel junction behavior. In fact, the n^+-GaAs/p^+-Si heterojunction does not show diode characteristics but has a resistance-like characteristics in our experiments. Although it increases the series resistance and decreases the fill factor (FF) of the tandem solar cell slightly, it does not cause a serious effect on the performance of the tandem solar cell.

4-3-2. $Al_xGa_{1-x}As$/Si tandem solar cells

Fig.4-6 shows the efficiency contour graphics for $Al_xGa_{1-x}As$/Si tandem solar cells. The theoretical optimal value (x) of Al composition in $Al_xGa_{1-x}As$ top cell is about 0.2, but the quality of the AlGaAs layer was degraded with increase of x rapidly in fact. Using growth sequence (b), we fabricated an $Al_xGa_{1-x}As$/Si tandem solar cell in the two-terminal configuration for various x. Table 4-3 summarizes the characteristics of the $Al_{0.22}Ga_{0.78}As$/Si and $Al_{0.15}Ga_{0.85}As$/Si

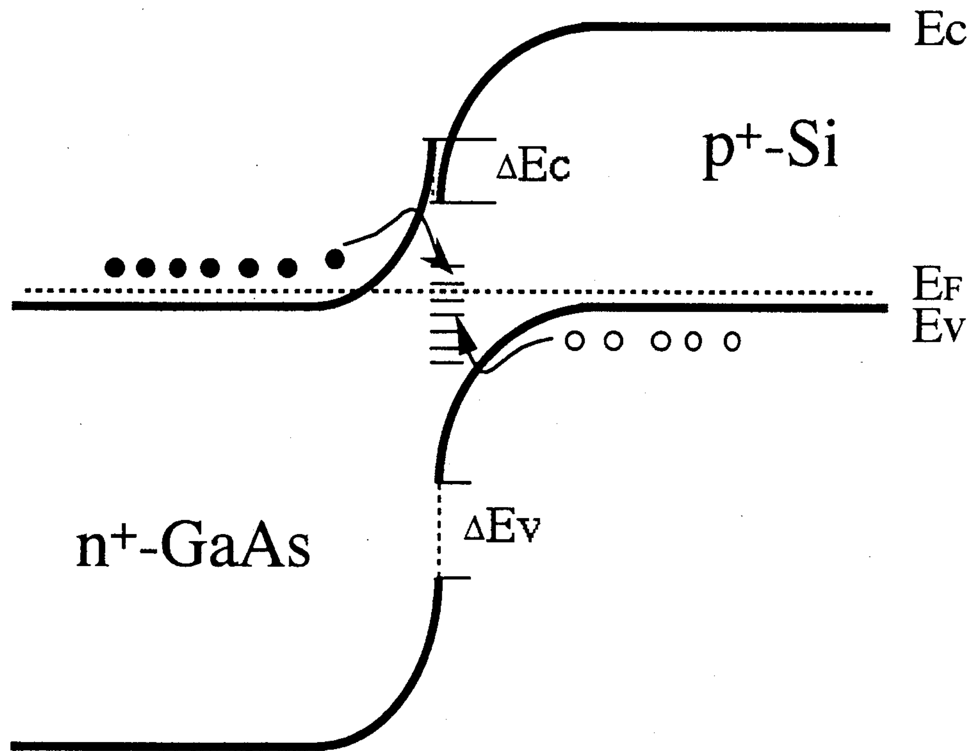

Fig. 4-5 A schematic band structure of the n^+-GaAs/p^+-Si tunnel heterojunction for the $Al_xGa_{1-x}As$/Si tandem solar cell.

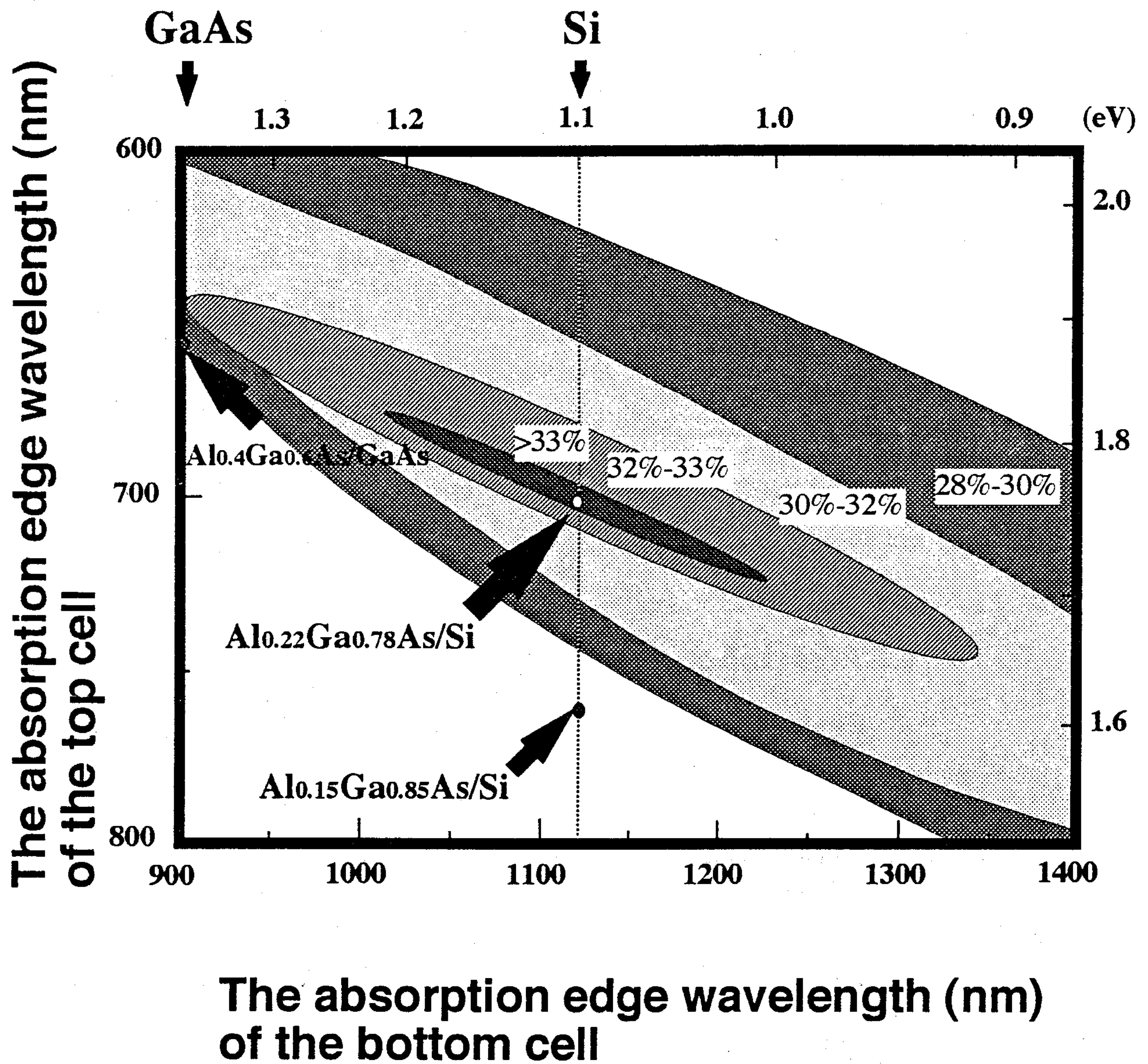

Fig. 4-6 The AMO calculated efficiency contour graphics for $Al_xGa_{1-x}As/Si$ two-terminal tandem solar cells.

tandem solar cells. Voc increases with x of Al composition, but Jsc decreases because the band-gap energy of $Al_xGa_{1-x}As$ increases with Al composition. The conversion efficiency of the top cell decreases with increasing x, and inversely, that of the Si bottom cell increases. In the case of the two-terminal configuration, Voc of the tandem cell is equal to the sum of that of the top cell and the bottom cell, Jsc of the tandem cell takes a smaller one as the top cell and the bottom cell are connected in series.

Jsc of the $Al_{0.22}Ga_{0.78}As$ has a lower value than that of the Si bottom cell, it resulted in low efficiency for the two-terminal configuration (13.3%) than the four-terminal configuration (17.7%). The efficiency of the $Al_{0.22}Ga_{0.78}As$ top cell on Si is much lower than that grown on GaAs substrate.[9),10)] There are mismatches in the lattice constants and thermal expansion coefficients of the two materials. These cause a high density of dislocations, which act as recombination centers and degenerate the crystalline quality of the AlGaAs layer seriously.

From Table 4-3, it can been seen that Jsc of the $Al_{0.15}Ga_{0.85}As$ top cell is close to that of the bottom cell on the point of current matching. Therefore, the $Al_{0.15}Ga_{0.85}As$/Si tandem solar cell appears to have the highest efficiency among the $Al_xGa_{1-x}As$/Si tandem solar cells. Fig. 4-7 shows the quantum efficiency of the $Al_{0.15}Ga_{0.85}As$/Si tandem cell.

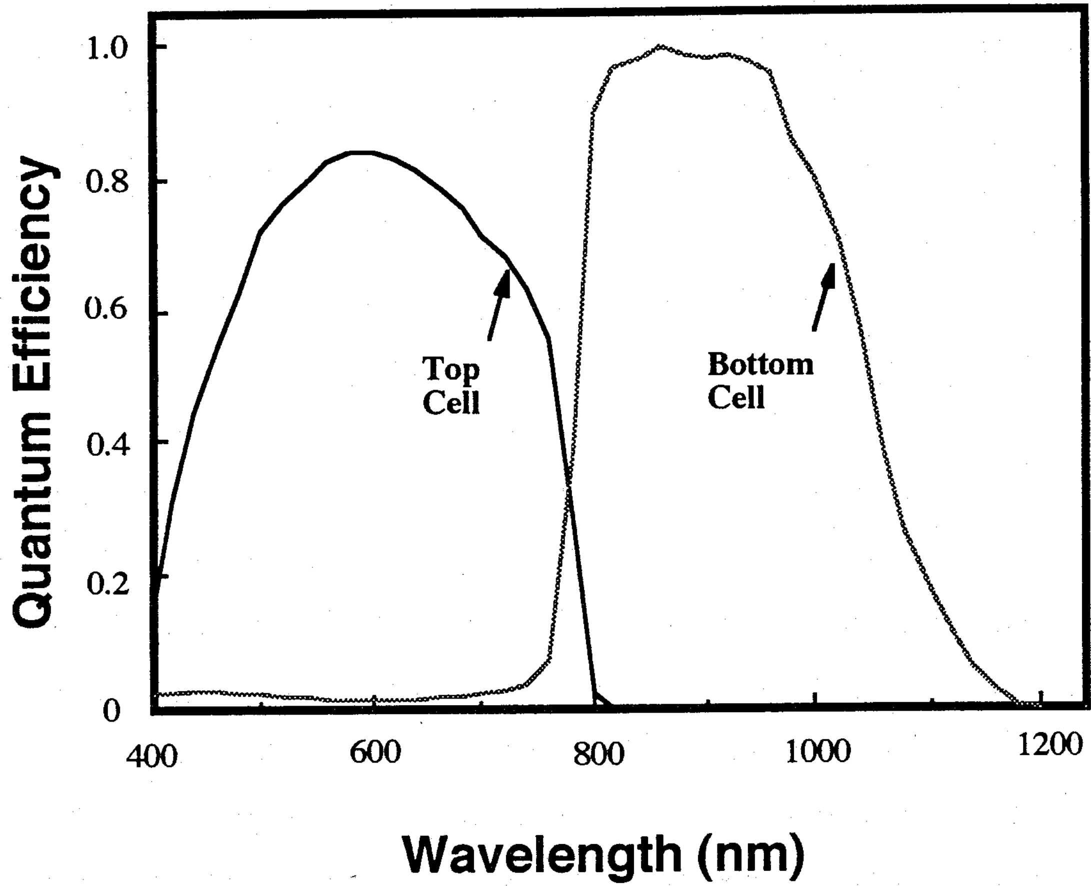

Fig. 4-7 The quantum efficiency of the $Al_{0.15}Ga_{0.75}As/Si$ two-terminal tandem solar cell.

Table 4-3
Photovoltaic characteristics of the $Al_{0.22}Ga_{0.78}As/Si$ and $Al_{0.15}Ga_{0.85}As/Si$ tandem solar cells.

Solar cells		Jsc (mA/cm^2)	Voc (V)	FF (%)	η (%)
$Al_{0.15}Ga_{0.85}As/Si$ tandem cell	top cell	21.8	0.960	71.8	11.1
	bottom cell	25.3	0.580	82.1	8.92
	2-term. tandem cell	22.0	1.51	77.3	19.0
	4-term. tandem cell				20.0
$Al_{0.22}Ga_{0.78}As/Si$ tandem cell	top cell	14.6	1.02	72.9	8.05
	bottom cell	28.4	0.579	79.7	9.69
	2-term. tandem cell	14.8	1.55	75.7	13.3
	4-term. tandem cell				17.7

Figure 4-8 shows the I-V characteristics of the $Al_{0.15}Ga_{0.85}As/Si$ tandem solar cell. It is clear that the Jsc of the two-terminal tandem cell is still limited to that of the top cell because the Jsc of the top cell is slightly smaller than that of the bottom cell. The active-area efficiency of 19.0% for the two-terminal configuration was achieved (Jsc=22.0 mA/cm^2, Voc=1.51 V, FF=77.3%). In the four-terminal configuration, the total conversion efficiency (the active area efficiency) of the $Al_{0.15}Ga_{0.85}As/Si$ tandem cell is as high as 20.0%.

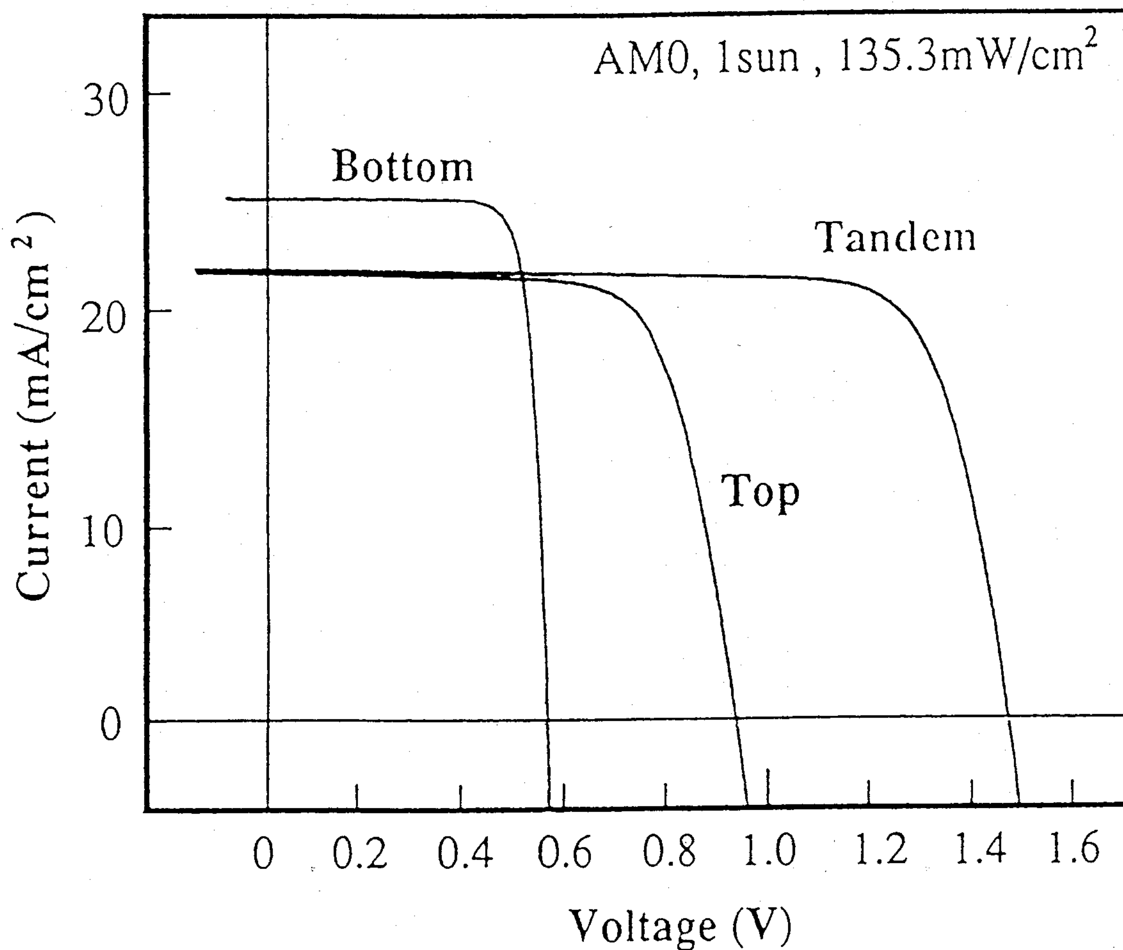

Fig. 4-8 Current-voltage characterics of the $Al_{0.15}Ga_{0.75}As/Si$ two-terminal tandem solar cell.

Chapter 4-4 Conclusion

The $Al_xGa_{1-x}As/Si$ tandem solar cells were designed and fabricated in a two-terminal configuration.

The quantum efficiency of the Si bottom cell was improved clearly by the BSF structure in the long-wavelength region, and the conversion efficiency of the Si bottom cell is increased.

Using a growth sequence with a high growth temperature (800℃) and thermal cycle annealing process of high temperature (300～ 900 ℃), the dislocation density of the $Al_xGa_{1-x}As$ top cell was decreased, resulting in the improvement of the conversion efficiency. When x of the Al composition of the AlGaAs top cell is 0.15, Jsc of the top cell is approximately close to that of the Si bottom cell. The active-area efficiencies of 19.0% and 20.0% for $Al_{0.15}Ga_{0.85}As/Si$ tandem solar cells (Jsc=22.0 mA/cm^2, Voc=1.51 V, FF=77.3%) with two-terminal and four-terminal configuration, respectively, have been obtained at 1sun, and AM0 measurement conditions. This is the highest efficiency for a monolithic AlGaAs/Si tandem solar cell ever reported.

The characteristics of the connector between the top cell and the bottom cell are also analyzed. The n-GaAs/p-Si heterojunction has tunnel junction properties in the experiment.

References

1) J. C. C. Fan, B-Y. Tsaur and B. J. Palm: *Conf. Rec. 16th IEEE Photovoltaic Specialists Conf.* (San Diego, USA, 1982) p. 692.

2) B. C. Chung, G. F. Virshup, S. Hikido and N. R. Kaminar: Appl. Phys. Lett. **55** (1989) 1741.

3) J. M. Olson, S. R. Kurtz and A. E. Kibbler: Appl. Phys. Lett. **56** (1990) 1990.

4) M. W. Wanlass, J. S. Ward, H. A. Emery and N. S. Coutts: *Proc. of the 23rd IEEE Photovoltaic Specialists Conf.* (Louisville, USA, 1993) p. 621.

5) L. D. Partain, M. S. Kuryla, R. E. Weiss, G. Werthen, G. F. Virshup, H. F. MacMillan, H. C. Hamaker and D. L. King: *Proc. of the 19th IEEE Photovoltaic Specialists Conf.* (USA, 1987) p. 1504.

6) K. A. Bertness, S. R. Kurtz, D. J. Firedman, A. E. Kibbler C. Kramer and J. M. Olson: Appl. Phys. Lett. **65** (1994) 989.

7) R. Y. Loo, and G. S. Kamath: *Proc. of the 20th IEEE Photovoltaic Specialists Conf.* (Las Vegas, USA, 1991) p. 635.

8) M. L. Timmons, R. Venkatasubramanian, P. A. Iles and C. L. Chu: *Proc. of 11th SPRAT, 1991, NASA Conf. Pub.* No.3121, p.37-1.

9) R. Venkatasubramanian, M. L. Timmons, T. S. Colpitts, J. Hancock, J. Hills and J. A. Hutchby: *Proc. of the 23th IEEE Photovoltaic Specialists Conf.* (Louisville, USA,

1993) p. 752.

10) K. Zahraman, Jean-C. Guillaume, G. Nataf, B. Beaumont, M. Leroux and P. Gibart: Jnp. J. Appl. Phys. **33** (1994) 5807.

11) J. M. Olson, S. R. Kurtz, A. E. Kibbler and P. Faine: *Proc. of the 21st IEEE Photovoltaic Specialists Conf.* (Florida, USA, 1990) p. 27.

12) R. Venkatasubramanian, M. L. Timmons, T. S. Colpitts, J. Hancock, J. Hills: Solar Cells, **30** (1991) 345.

13) G. W.'t Hooft, C. van Opdorp, H. Veenvliet and A. T. Vink: J. Crystal Growth, **55** (1981) 173.

14) A. G. Milens and D. L. Feucht: *Heterojunctions and Metal-Semiconductor Junctions* (Academic Press, New York, 1972).

Chapter 5. Application to integrated wavelength division sensor

5-1. Introduction

In recent years, the hetero-epitaxial growth technology of GaAs on Si has received a great attention for the possible monolithic integration of GaAs optoelectronic devices on Si VLSI.[1-3] In this chapter, we demonstrate a new application of GaAs/Si to a sensor that can indicate the wavelength of monochromatic light directly. This kind of sensor is required to monitor or control the tunable laser e.g. Ti: sapphire laser. The sensor consists of two photodiodes, i.e., the GaAs top photodiode and the Si bottom photodiode. A GaAs p-n junction photodiode was grown on a Si p-n junction photodiode by MOCVD technique. GaAs and the intermediate layer between the GaAs layer and the Si layer play a role of a short-wavelength cut filter for the bottom Si photodiode. The spectral response of the top photodiode decreases and the light that penetrates to the bottom Si photodiode increases as the wavelength of the input light increases toward the absorption edge of GaAs. In this wavelength region, photocurrents of the top photodiode and the bottom photodiode depend on the wavelength of the input light. This characteristic can be used to measure the wavelength of the incident monochromatic light without using any external filter or dispersive elements.[4] As the sensor is integrated monolithically on Si wafer, the size of the sensor can be made small and the Si electronic circuit to process the data could be integrated monolithically, too.

5-2. Design and Structure of the sensor

The crystal quality of GaAs is poor near the hetero-interface because of the existence of thermal expansion coefficient and lattice mismatch between GaAs and Si. A thick GaAs epitaxial layer makes the crystal quality better, but the light with wavelength shorter than the absorption edge is little able to penetrate to the bottom photodiode. This problem can be solved by using a wide-band-gap intermediate layer between GaAs and Si.

In order to make the incident light of wavelength from 600 nm to 900 nm penetrate through the top photodiode and the intermediate layer between the top sensor and the bottom sensor, we have designed a GaAs photodiode with a very thin GaAs active layer for the top sensor and an $Al_{0.4}Ga_{0.6}As$ intermediate layer as shown in Fig. 5-1. An $Al_xGa_{1-x}As$ layer with the Al content varying from 0.25 to 0.05 was grown between the active layer of top GaAs sensor and $Al_{0.4}Ga_{0.6}As$ layer. P^+ - $Al_xGa_{1-x}As$ graded-band-gap layer with Al content varying from 0.05 to 0.25 was also grown between $Al_{0.85}Ga_{0.15}As$ window layer and the GaAs active layer. The electric field produced by the graded-band-gap layer reduces the recombination of photo-carriers at the interface between the $Al_{0.85}Ga_{0.15}As$ window layer and the p-GaAs active layer, and increase the collection efficiency of the photo-carriers in the top photodiode.

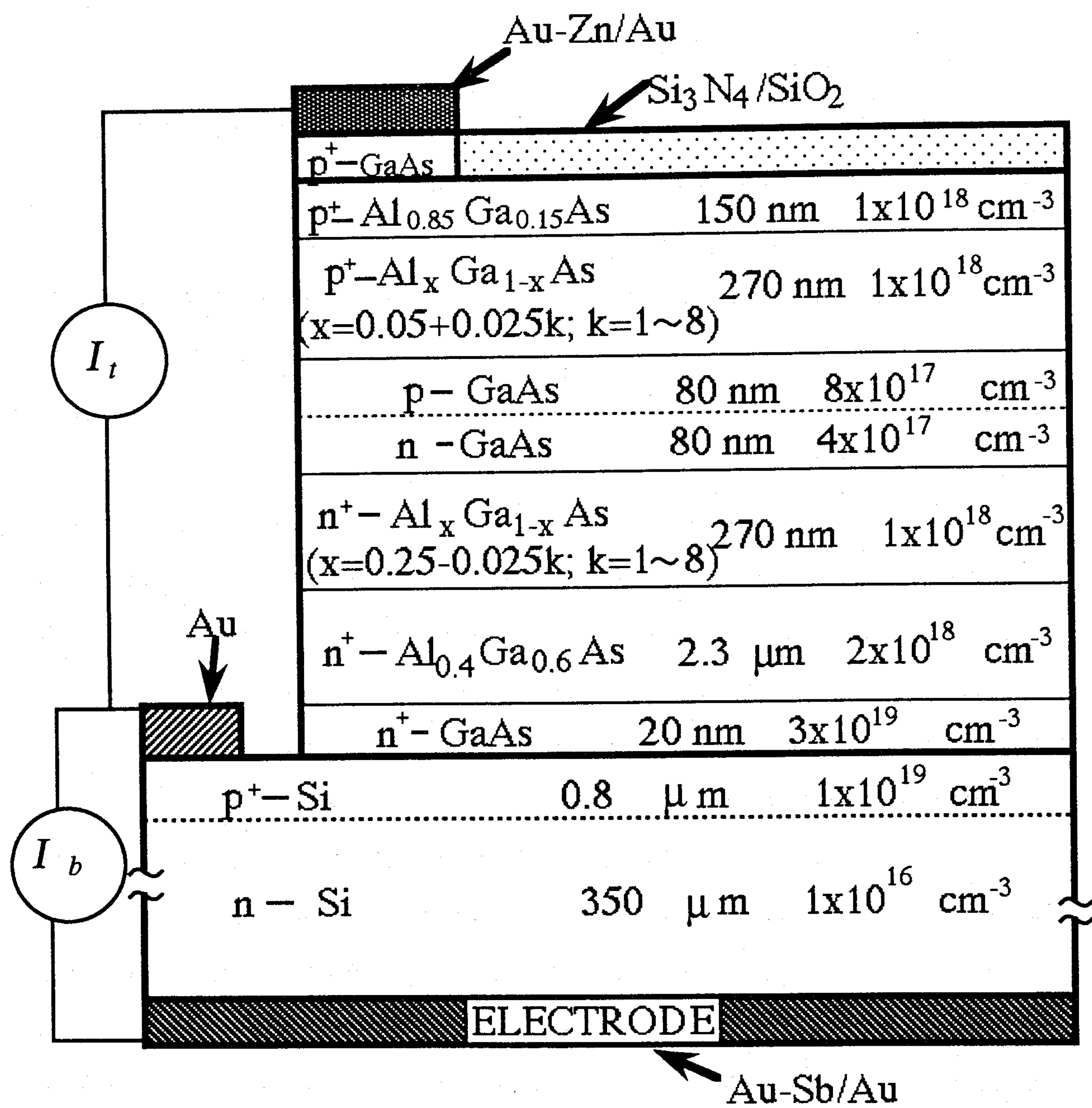

Fig. 5-1. The schematic cross-sectional structure of integrated wavelength-division sensor using GaAs on Si.

5-3. Sample fabrication

The bottom photodiode was fabricated by the thermal diffusion of B at 1000 ℃ in n-type (100) Si wafer with misorientation of 2° towards [011]. After the p-n junction formation, the Si wafer was slightly etched by the acid solution ($H_2SO_4:H_2O_2:H_2O$= 4:1:1 + HF:H_2O=1:1) and followed by heat treatment at 1000 ℃ in H_2 atmosphere to remove the oxide on it. On this Si wafer, n^+ -GaAs buffer layer and the top photodiode structure were grown by MOCVD using two-step growth technique. The top photodiode consists of n^+ -GaAs buffer layer, n^+-$Al_{0.4}Ga_{0.6}As$ intermediate layer, n^+ -$Al_xGa_{1-x}As$ buffer layer, n and p-GaAs active layer, p^+-$Al_xGa_{1-x}As$ graded-band-gap layer, $Al_{0.85}Ga_{0.15}As$ window layer and p^+- GaAs contact layer. After n^+ -$Al_{0.4}Ga_{0.6}As$ layer was grown, thermal cycle annealing treatment from 300 ℃ to 850 ℃ was carried out three times in H_2 + AsH_3 atmosphere. The crystal quality was evaluated for 2.7 μm-thick GaAs grown on Si by the two-step growth method with the thermal cycle treatment. The etch pit density revealed by molten KOH etching was $1.5x10^7$ cm^{-2} and the hole diffusion length measured by the electron beam induced current (EBIC) was 0.9 μm. The Si_3N_4 /SiO_2 layers were evaporated for as surface anti-reflection films. Three electrodes were formed on p^+ -GaAs, p^+ -Si and n-Si, respectively.

5-4. Output properties

The quantum efficiency of the top GaAs photodiode and the bottom Si photodiode are shown in Fig.5-2. Both photocurrents of the bottom photodiode I_b and the top photodiode I_t are a function of the wavelength of incident light. If we regard $S = (I_b-I_t)/(I_b+I_t)$ as an output, it has a good linear relationship with wavelength in the region from 620 nm to 880 nm. This characteristic of the 3-terminal monolithic GaAs/Si sensor is quite suitable for the measurement of the wavelength of monochromatic light. In this wavelength region, the wavelength λ is expressed by S as follows:

$$\lambda\ (\mathrm{nm}) = 729 + 132S + \varepsilon \qquad (1)$$

where ε is an error and $|\varepsilon|$ is less than 2 nm. For wider wavelength region, nonlinear terms must be included. The output properties of the GaAs/Si sensor vs. the wavelength of the incident light is shown in Fig. 5-3. The wavelength of monochromatic light can be known from the output S.

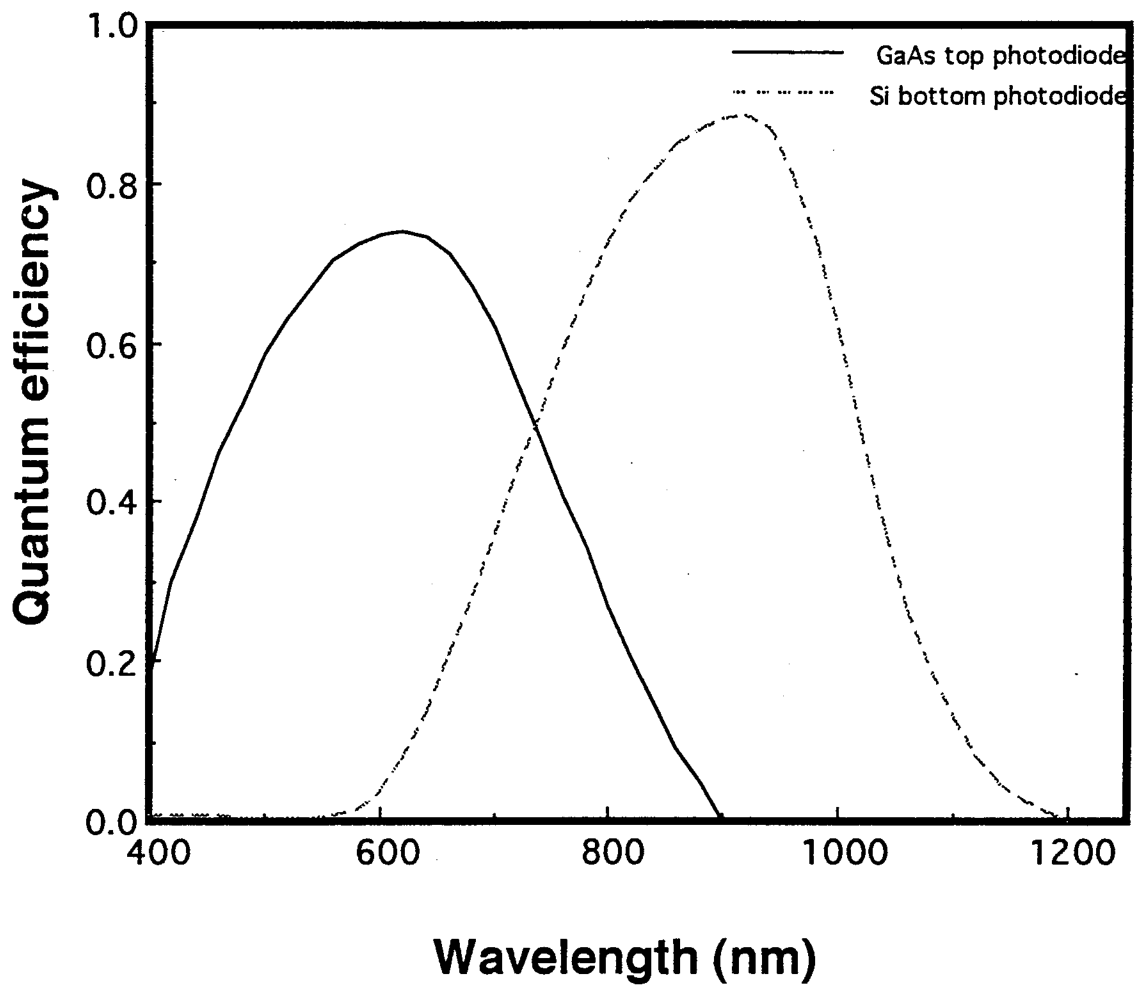

Fig. 5-2. Spectral quantum efficiency of integrated wavelength-division sensor using GaAs photodiode and Si photodiode.

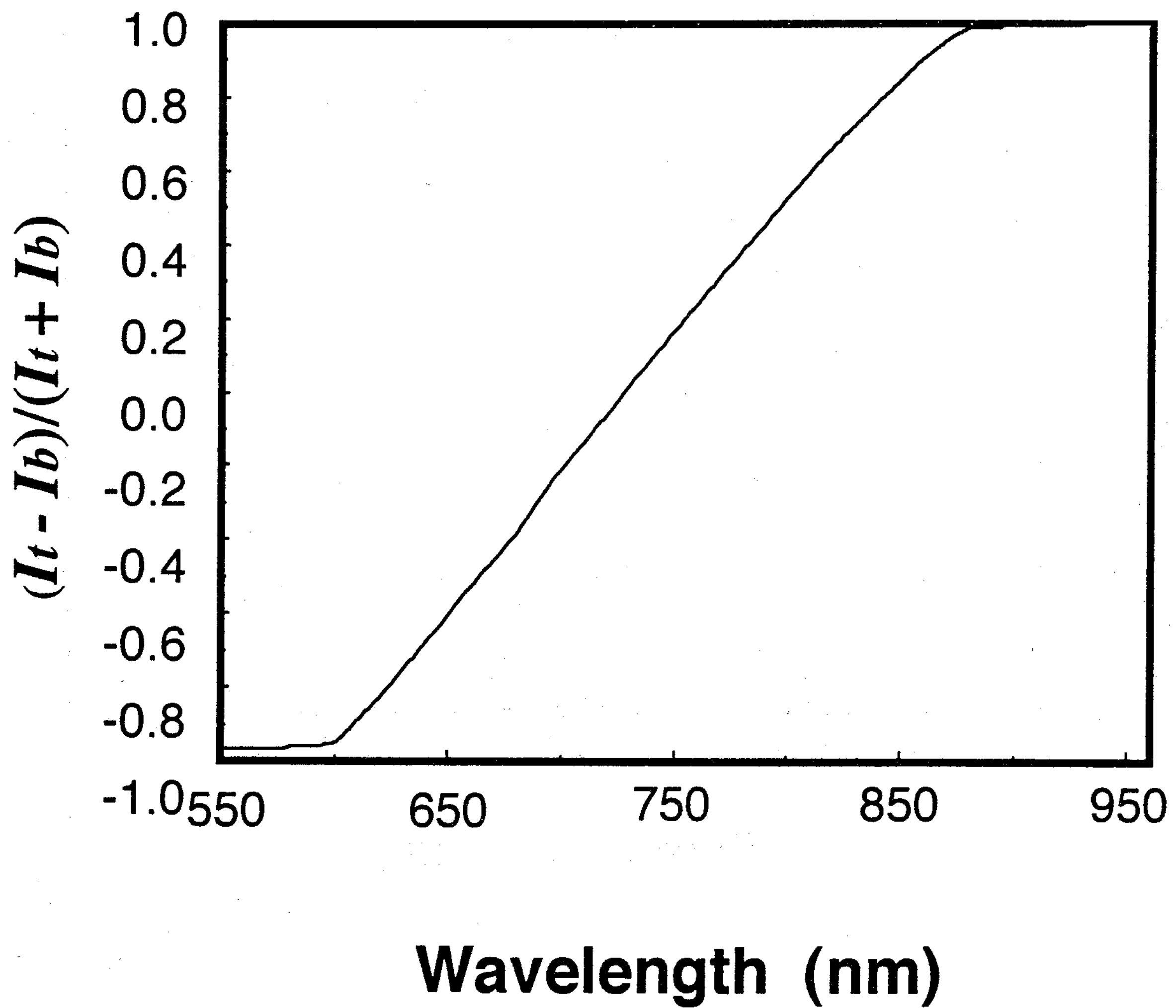

Fig. 5-3. Normalized difference spectrum of photocurrents of integrated sensor using GaAs on Si.

5-5. Conclusion

A new integrated wavelength-division photo-sensor using GaAs/Si is proposed and fabricated by MOCVD. It can be conveniently used to measure the wavelength of monochromatic light without using any filter or dispersive elements. Normalized difference of the photocurrents of this sensor is linearly dependent on the wavelength of the incident monochromatic light from 600 nm to 880 nm. Signal processing circuits can be also integrated on the same Si wafer.

References

1) R. Fisher, W. T. Masselink, J. Klem, T. Henderson, T. C. McGlinn, M. V. Klien, H. Morkoc, T. J. Mazur, J. Washburn: J.Appl.Phys. **58** (1985) 374.

2) K. Ishida, M. Akiyama and S. Nishi: Jpn.J.Appl.Phys. **25** (1986) L288.

3) T. Egawa, T. Jimbo and M. Umeno: *Technical Digest of 1991 IEDM* (Washington, DC) P.953.

4) H. Kato, S. Norinaga, A. Yoshida and T. Arizumi: J. Phys. E. **9** (1976) 1070.

Chapter 6. Summary

This research work is aimed at systematic experimental and theoretical study of the high efficiency $Al_xGa_{1-x}As/Si$ tandem solar cells. The performances of $Al_xGa_{1-x}As/Si$ tandem solar cells dependent on the device parameters were studied in detail theoretically, and high conversion efficiency of 20% for the tandem solar cell has been achieved in 1 sun, AM0 conditions experimentally.

In Chapter 1, the history and developments of the modern solar cells were reviewed briefly. Heteroepitaxial growth of GaAs on Si, its application and the purpose of this dissertation were described. The important results obtained by experiments up to the present are also summarized in a table.

In Chapter 2, the material properties and the parameters of GaAs, AlGaAs, Si and GaAs-on-Si were reviewed in general, and the empirical expressions used in the calculation were described in detail. The theoretical calculation and design for high efficiency $Al_xGa_{1-x}As/Si$ tandem solar cells were carried out. The structure design and the parameter optimization are concentrated on GaAs/Si three-terminal tandem solar cells and AlGaAs/Si two-terminal tandem solar cells, respectively. The calculations are based on the assumption that the reflection of solar cells is zero and AlGaAs window layer has no photo-absorption losses.

For GaAs/Si three-terminal tandem solar cells, the minority-carrier parameters used in the calculation are considered as the functions of the dislocations and the doping

concentrations. Effects of the dislocation density (N_d) in GaAs-on-Si, the base layer doping concentration (N_D), junction depth (X_j), electric field strength (E) in the emitter layer on photovoltaic properties of the GaAs top cell were analyzed. From these results, it has been demonstrated that the AM0 efficiency of the GaAs top cell on Si about 25% can be expected by reducing the dislocation density below 1×10^5 cm^{-2}, employing a n-GaAs base layer with the carrier concentration of about 1×10^{16} cm^{-3}, using a shallow p-n junction depth about 300 nm and a graded bandgap emitter layer with the strong electric field ($E\geqq14500$ V/cm). It is important to improve the spectral response of the Si bottom cell in the long wavelength region. Reducing the recombination velocity of back surface (S_b) by passivation, using a Si substrate with high resistivity (~50 Ω·cm) and BSF structure, the efficiency of the Si bottom cell will be more than 7%. So that, combing the efficiency of the top cell and the bottom cell, the conversion efficiency over 31% can be achieved in theory for GaAs/Si three-terminal tandem solar cell with the optimized parameters and the improvement of quality of the heteroepitaxial layer on Si (the dislocation density is lower than 10^5 cm^{-2}). The performances of $Al_xGa_{1-x}As$/Si two-terminal tandem solar cells were analyzed from the point of the photocurrent matching between the top cell and the bottom cell, assuming that the AlGaAs-on-Si material quality is good as AlGaAs-on-GaAs. When Al composition is about 0.21, the photocurrent matching between the top cell and the bottom cell could be satisfied (Jsc=30 mA/cm^2) and the conversion efficiency (1sun, AM0) of

32.3% could be obtained in theory.

In Chapter 3, GaAs/Si three-terminal monolithic tandem solar cells fabricated by MOCVD were studied. The "As auto-doping effect" and the effects of the GaAs growth on the Si bottom cells were investigated by the SIMS and EBIC. Using a graded-bandgap-layer of $Al_xGa_{1-x}As$, the quantum efficiency of GaAs top cell was considerably improved within wavelength from 460 nm to 860 nm. Short-circuit current of the GaAs top cell increased from 21.1 mA/cm^2 to 30.7 mA/cm^2. The performance of the GaAs top cell has been improved further when the GBEL structure of AlGaAs is growth at 800 ℃, the conversion efficiency is up to 16% (AM0, active-area efficiency). And then, the characteristics of the connector between the top cell and the bottom cell are analyzed. An isotype n-n/ GaAs-Si heterojunction connector for the three-terminal GaAs/Si solar cell behaves as a resistance with very small value. For the Si bottom cell, the quantum efficiency in the long wavelength is enhanced by using p-Si substrate with proper resistivity (10 Ω·cm) and BSF structure. The total conversion efficiency (active-area efficiency) of 19.5% and 19.9% under 1 sun, AM0 measurement conditions have been achieved by the GaAs/Si three-terminal monolithic tandem solar cell with the GaAs and the AlGaAs buffer layer, respectively.

In Chapter 4, the characteristics of the $Al_xGa_{1-x}As$/Si two-terminal tandem solar cells were studied. The quantum efficiency of the Si bottom cell was improved clearly by the BSF structure in the long-wavelength region, and the conversion efficiency of the Si bottom cell is increased.

Using a growth sequence with a high growth temperature (800℃) and thermal cycle annealing process of high temperature (300～900℃), the dislocation density of the $Al_xGa_{1-x}As$ top cells was decreased. When x of the Al composition of the AlGaAs top cell is 0.15, Jsc of the top cell is approximately close to that of the Si bottom cell. The active-area efficiencies (1sun, AM0) of 19.0% and 20.0% for $Al_{0.15}Ga_{0.85}As$/Si tandem solar cells have been obtained with two-terminal and four-terminal configuration, respectively. This is the highest efficiency for a monolithic AlGaAs/Si tandem solar cell ever reported. The characteristics of the connector between the top cell and the bottom cell are also analyzed. The n-GaAs/p-Si heterojunction has tunnel junction properties in the experiment.

In Chapter 5, a new integrated wavelength-division photo-sensor using GaAs/Si is proposed. It can be conveniently used to measure the wavelength of monochromatic light without using any filter or dispersive elements. Normalized difference of the photocurrents of this sensor is linearly dependent on the wavelength of the incident monochromatic light from 600 nm to 880 nm. Signal processing circuits can be also integrated on the same Si wafer.